arXiv:1410.8809v3 [cond-mat.mes-hall] 22 Feb 2015

Quantum capacitance and compressibility of graphene: The role of Coulomb interactions

Yu.E. Lozovik,[1,2,3,4,*] A.A. Sokolik,[1,2] and A.D. Zabolotskiy[1,3]

[1] *Institute for Spectroscopy, Russian Academy of Sciences, 142190 Troitsk, Moscow, Russia*
[2] *MIEM at National Research University HSE, 109028 Moscow, Russia*
[3] *All-Russia Research Institute of Automatics, 127055 Moscow, Russia*
[4] *National Research Nuclear University MEPHI, 115409 Moscow, Russia*

Many-body effects on quantum capacitance, compressibility, renormalized Fermi velocity, kinetic and interaction energies of massless Dirac electrons in graphene, induced by Coulomb interactions, are analyzed theoretically in the first-order, Hartree-Fock and random phase approximations. Recent experimental data on quantum capacitance and renormalized Fermi velocity are analyzed and compared with the theory. The bare Fermi velocity and the effective dielectric constants are obtained from the experimental data. A combined effect of Coulomb interactions and Gaussian fluctuations of disorder potential is considered.

PACS numbers: 73.22.Pr, 71.10.-w, 71.45.Gm, 73.21.-b

I. INTRODUCTION

Discovery of graphene, a two-dimensional carbon material with effectively massless electrons, stimulated new fundamental and applied studies in solid state physics [1–3]. In recent years, considerable attention has been attracted to the problem of compressibility and quantum capacitance of graphene, which is connected both with fundamental physics of the Coulomb-interacting gas of massless electrons and with possible applications of graphene in electronics and energy storage technologies.

In the early experiments [4] on graphene electron compressibility, results consistent with the model of a non-interacting Dirac electron gas were reported. The linear dispersion and chirality of graphene electrons were proposed as possible causes of the apparent absence of electron interaction signatures [5].

The recent experiments [6–8] on measuring electron compressibility or quantum capacitance in high-quality graphene samples revealed signatures of electron interactions, in consistency with the many-body calculations [9–13] of these quantities. The observed interaction-induced effects are closely related to the logarithmic renormalization of the electron Fermi velocity in graphene in the vicinity of the charge neutrality point (CNP), which was observed by different experimental groups [14–18] and considered in theoretical literature (see [19], reviews [1–3] and literature cited in [20]).

A random potential, arising in real graphene samples due to charged impurities and corrugations, manifests itself in formation of electron-hole puddles [4, 18, 21–23] and qualitatively changes graphene physics at low carrier densities near CNP. Disorder has been proposed as a source of the observed nonvanishing compressibility and quantum capacitance of graphene at CNP [8, 23–29].

*Electronic address: lozovik@isan.troitsk.ru

To describe the experimentally measured dependencies of compressibility and quantum capacitance on electron density the model of Gaussian fluctuations of the disorder potential was successfully used [23, 29–33]. The random phase approximation with a polarizability, modified by disorder, was used to calculate the compressibility in [12].

In the present article, we perform a theoretical study of quantum capacitance and related properties of graphene in presence of Coulomb interactions in the first-order approximation (FOA), Hartree-Fock approximation (HFA) and random phase approximation (RPA). In order to obtain the bare Fermi velocity v_F, we analyze the recent experimental data on quantum capacitance and renormalized Fermi velocity [6–8, 18]. Influence of Coulomb interactions on quantum capacitance and renormalized Fermi velocity (see Sec. III for its definition) as well as kinetic and interaction energies of an electron gas in graphene are studied in FOA, HFA and RPA. A combined effect of Coulomb interaction and disorder on these quantities is studied within the model of Gaussian electrostatic potential fluctuations.

We show that both HFA and RPA are in close agreement with the experiments at $v_\mathrm{F} \approx 0.9 \times 10^6\,\mathrm{m/s}$, although HFA requires much larger effective dielectric constants of surrounding media to simulate the screening, lacking in this approximation. The influence of Coulomb interactions on the properties of the electron gas has two major features: exchange effects push the Fermi velocity to higher values and the quantum capacitance to lower values; correlation effects partly compensate the exchange ones. The renormalized Fermi velocity increases up to 50 % at the lowest achievable densities near CNP and by 10–20 % away from CNP. The quantum capacitance is typically reduced by 10–15 %, although it can be described within the non-interacting model with $v_\mathrm{F} \approx 1.1 \times 10^6\,\mathrm{m/s}$. In presence of disorder, a nonzero quantum capacitance appears at CNP, in agreement with the experiments, whereas the renormalized Fermi velocity turns out to be suppressed near CNP.

The article is organized as follows. Is Sec. II we present theoretical models used to calculate the characteristics of the electron gas. In Sec. III we perform an analysis of experimental data. Many-body effects of Coulomb interactions on the properties of the electron gas in graphene are studied in Sec. IV. Influence of disorder is considered in Sec. V, and Sec. VI concludes the article.

II. THEORETICAL MODELS

We start with a description of the electron gas in graphene in terms of a grand canonical ensemble when the temperature T, chemical potential μ and area of the system S are the controlling parameters. Physically this corresponds to a flake of graphene, brought in a contact with a conductor, specifying μ. Under these conditions, the system tends to an equilibrium, where the thermodynamic potential $\Omega = E - T\mathfrak{S} - \mu N$ attains a minimum (E and $\mathfrak{S}$ are the internal energy and entropy of the electron gas, N is the mean number of electrons in the system). The electron surface density, or concentration, $n = N/S$, is given by

$$n = -\frac{1}{S}\frac{\partial\Omega}{\partial\mu}. \tag{1}$$

The compressibility κ and the quantum capacitance per unit area $C_{\rm Q}$ can be calculated as:

$$\kappa = \frac{1}{n^2}\frac{dn}{d\mu}, \qquad C_{\rm Q} = e^2\frac{dn}{d\mu} \tag{2}$$

(sometimes merely $d\mu/dn$ is referred to as the inverse compressibility [8, 9]). The quantum $C_{\rm Q}$ and classical $C_{\rm C}$ capacitances form the total capacitance $C_{\rm tot}$ as $C_{\rm tot}^{-1} = C_{\rm Q}^{-1} + C_{\rm C}^{-1}$, thus the smaller of them dominates. In particular, $C_{\rm tot}$ acquires a significant quantum correction when $C_{\rm Q} \ll C_{\rm C}$ (see insets in Fig. 6).

In a noninteracting system, the thermodynamic potential Ω_0 in the $T \to 0$ limit is:

$$\Omega_0 = g\sum_{\mathbf{p}\gamma}(\epsilon_{\mathbf{p}\gamma} - \mu)f(\epsilon_{\mathbf{p}\gamma}), \tag{3}$$

where $\epsilon_{\mathbf{p}\gamma} = \gamma v_{\rm F}|\mathbf{p}|$ is the one-particle energy of an electron in graphene with the momentum $\mathbf{p}$ in a conduction or valence band at $\gamma = \pm 1$ respectively; $v_{\rm F}$ is the bare Fermi velocity; $g = 4$ is the degeneracy factor over spin and valleys; and $f(\epsilon) = \Theta(\mu - \epsilon)$ is the occupation number for a state with the energy ϵ at $T \to 0$, where $\Theta(x)$ is the unit step function.

The electron density in the noninteracting graphene is determined through (1) and (3) as:

$$n_0(\mu) = {\rm sgn}(\mu)\frac{g\mu^2}{4\pi v_{\rm F}^2} \tag{4}$$

($\hbar \equiv 1$). Here μ and n are counted, respectively, from CNP and from the background electron density of the filled valence band; thus n is positive or negative in, respectively, electron- or hole-doped graphene.

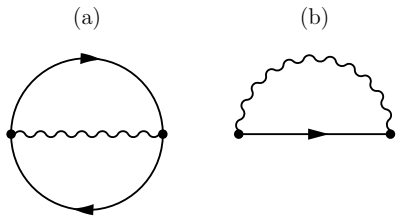

FIG. 1: (a) The first-order exchange diagram for $\delta\Omega$ (5). (b) The first-order exchange diagram for the self-energy (7).

Change of the thermodynamic potential $\delta\Omega = \Omega - \Omega_0$ when interactions are switched on can be calculated as a sum of closed connected diagrams [34, 35].

The simplest approximation to calculate Ω is the first-order approximation, where we take into account only the first-order exchange diagram, shown in Fig. 1(a). The resulting first-order correction to the thermodynamic potential is:

$$\delta\Omega_1 = -\frac{g}{2S}\sum_{\mathbf{p}\mathbf{p}'\gamma\gamma'} V_{\mathbf{p}-\mathbf{p}'}F_{\mathbf{p}\gamma\mathbf{p}'\gamma'}f(\epsilon_{\mathbf{p}\gamma})f(\epsilon_{\mathbf{p}'\gamma'}), \tag{5}$$

where $V_{\mathbf{q}} = 2\pi e^2/\varepsilon|\mathbf{q}|$ is the Coulomb potential, ε is the effective dielectric permittivity of a surrounding medium, $F_{\mathbf{p}\gamma\mathbf{p}'\gamma'} = [1 + \gamma\gamma'\cos(\hat{\mathbf{p}\mathbf{p}'})]/2$ is the angular factor, accounting for an overlap of two-component spinor parts of electron wave functions.

From (1) and (5) we get the first-order correction $\delta n_1 = n - n_0$ to the electron density:

$$\delta n_1(\mu) = -\frac{g|\mu|}{2\pi v_{\rm F}^2}\Sigma^{(1)}_{|\mu|/v_{\rm F},{\rm sgn}(\mu)}, \tag{6}$$

where

$$\Sigma^{(1)}_{\mathbf{p}\gamma} = -\frac{1}{S}\sum_{\mathbf{p}'\gamma'} V_{\mathbf{p}-\mathbf{p}'}F_{\mathbf{p}\gamma\mathbf{p}'\gamma'}f(\epsilon_{\mathbf{p}'\gamma'}) \tag{7}$$

is the $T \to 0$ limit of the electron first-order exchange self-energy, depicted in Fig. 1(b).

The explicit expressions for $\Sigma^{(1)}_{\mathbf{p}\gamma}$, calculated beyond the logarithmic term [19], were presented in [9, 10, 36–39]. This self-energy can be calculated exactly in terms of generalized hypergeometric functions, but its expansion

$$\Sigma^{(1)}_{|\mu|/v_{\rm F},{\rm sgn}(\mu)} = \frac{e^2\mu}{2\varepsilon v_{\rm F}}\left\{\frac{1}{2}\ln\Lambda + \ln 2 - \frac{1}{4} - \frac{2\mathcal{C}+1}{\pi} + \frac{{\rm sgn}(\mu)}{4\Lambda}\right\} \tag{8}$$

in powers of the dimensionless cutoff $\Lambda = v_{\rm F}p_{\rm c}/|\mu|$ ($p_{\rm c}$ is the cutoff momentum in the valence band, $\mathcal{C} \approx 0.916$ is Catalan's constant) up to Λ^{-1} is sufficiently accurate in the range $6 < \Lambda < \infty$, corresponding to the density

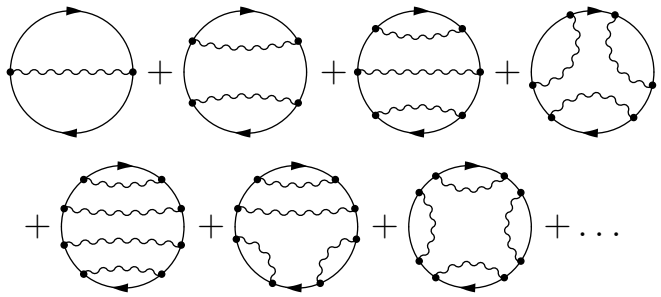

FIG. 2: The closed connected diagrams for $\delta\Omega$ in the Hartree-Fock approximation.

range $0 < |n| < 10^{14}\,\mathrm{cm}^{-2}$. Thus (6) and (8) allow to determine Ω and its derivatives in FOA.

The Hartree-Fock approximation, providing more accurate results than FOA, can be obtained by "dressing" the electron Green functions in Fig. 1(a) with exchange self-energy parts. Unfortunately, as is known [34], one cannot simply replace any bare Green function in closed diagrams by a Hartree-Fock one, because this would result in overcounting of the diagrams. In fact, in order to obtain HFA starting from the grand canonical ensemble, we need to calculate the infinite series of diagrams, depicted in Fig. 2, with each diagram having a numerical prefactor, dependent on its symmetry.[1]

To overcome this difficulty, we can calculate Ω by means of the Luttinger-Ward functional [40], where all excess diagrams, appearing in the "overcounted" thermodynamic potential, are exactly compensated by a simple expression. In this way, choosing the Hartree-Fock skeleton diagrams (Fig. 1), we can calculate (similarly to Appendix A in [41]) the thermodynamic potential in the $T \to 0$ limit:

$$\Omega_{\mathrm{HF}} = g\sum_{\mathbf{p}\gamma}\left(\epsilon_{\mathbf{p}\gamma} + \frac{\Sigma^{(\mathrm{HF})}_{\mathbf{p}\gamma}}{2} - \mu\right) f(\epsilon_{\mathbf{p}\gamma} + \Sigma^{(\mathrm{HF})}_{\mathbf{p}\gamma}), \quad (9)$$

where the Hartree-Fock self-energy is

$$\Sigma^{(\mathrm{HF})}_{\mathbf{p}\gamma} = -\frac{1}{S}\sum_{\mathbf{p}'\gamma'} V_{\mathbf{p}-\mathbf{p}'} F_{\mathbf{p}\gamma\mathbf{p}'\gamma'} f(\epsilon_{\mathbf{p}'\gamma'} + \Sigma^{(\mathrm{HF})}_{\mathbf{p}'\gamma'}). \quad (10)$$

The occupation numbers $f(\epsilon_{\mathbf{p}\gamma} + \Sigma^{(\mathrm{HF})}_{\mathbf{p}\gamma})$, entering into these equations, drop from 1 to 0 at the Fermi surface, where $p = p_{\mathrm{F}}$, $\gamma = \mathrm{sgn}(\mu)$. Applying (1) to (9) and subtracting the background electron density, we obtain

[1] Note that naive calculation of all of these diagrams except the first-order one directly at $T = 0$ will result in zero. Careful evaluation of these "anomalous" [40] or "rainbow" [20] diagrams should imply taking the $T \to 0$ limit only after calculating all of them at $T \neq 0$ and summing the full diagrammatic series.

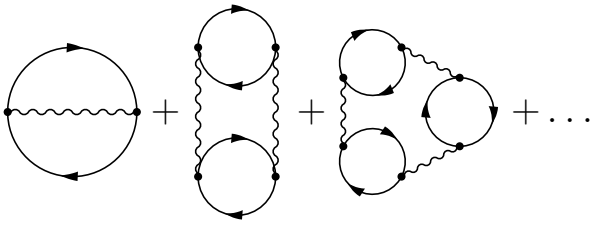

FIG. 3: The closed connected diagrams for $\delta\Omega$ in the random phase approximation.

the electron density in HFA:

$$n_{\mathrm{HF}}(\mu) = \frac{g}{S}\sum_{\mathbf{p}\gamma}\left[f(\epsilon_{\mathbf{p}\gamma} + \Sigma^{(\mathrm{HF})}_{\mathbf{p}\gamma}) - \Theta(-\epsilon_{\mathbf{p}\gamma})\right]. \quad (11)$$

In fact, the expressions (9)–(11) depend on p_{F}, rather than on μ, therefore it is more convenient to find the Fermi momentum p_{F} from the equation

$$\mu = \epsilon_{p_{\mathrm{F}},\mathrm{sgn}(n)} + \Sigma^{(1)}_{p_{\mathrm{F}},\mathrm{sgn}(n)} \quad (12)$$

and then use Eq. (11), rewritten in the form:

$$n_{\mathrm{HF}}(\mu) = \mathrm{sgn}(\mu)\frac{g p_{\mathrm{F}}^2}{4\pi}. \quad (13)$$

Here we used the equality $\Sigma^{(\mathrm{HF})}_{p_{\mathrm{F}},\mathrm{sgn}(n)} = \Sigma^{(1)}_{p_{\mathrm{F}},\mathrm{sgn}(n)}$, following from (7), (10) and (12). Solving (12)–(13) and integrating $n_{\mathrm{HF}}(\mu)$ according to (1), we can restore the thermodynamic potential in HFA.

The calculations in (9)–(13) may appear rather formal, especially in the light of similarity of (4) and (13), but they demonstrate the essential difference between the first-order and Hartree-Fock approximations: the latter is *self-consistent*, which means that it actually takes into account an infinite series of Feynman diagrams (Fig. 2) and deals with the renormalized electron dispersion $\epsilon_{\mathbf{p}\gamma} + \Sigma^{(\mathrm{HF})}_{\mathbf{p}\gamma}$ instead of $\epsilon_{\mathbf{p}\gamma}$.

The random phase approximation for calculating Ω becomes asymptotically exact in the limit $g \to \infty$ of large electron state degeneracy [42, 43]. It was also argued that RPA dominates in graphene because of taking into account all diagrams with infrared divergences [44]. Recently applicability of RPA has been confirmed by quick convergence of expansion in RPA-screened interaction [45]. The sum of diagrams for $\delta\Omega$ in this approximation, shown in Fig. 3, is (see also [11]):

$$\delta\Omega_{\mathrm{RPA}} = \frac{1}{2}\sum_{\mathbf{q}}\left\{T\sum_{\omega_k}\ln\left[1 - V_{\mathbf{q}}\Pi_{\mathbf{q}}(i\omega_k)\right] - nV_{\mathbf{q}}\right\}, \quad (14)$$

where $\omega_k = 2\pi T k$ are bosonic Matsubara frequencies. The polarizability of the electron gas in graphene $\Pi_{\mathbf{q}}(\omega)$ was calculated explicitly elsewhere at real [46, 47] and imaginary [11] frequencies.

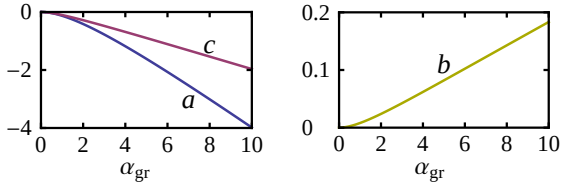

FIG. 4: The functions $a(\alpha_{gr})$, $b(\alpha_{gr})$ and $c(\alpha_{gr})$ in the expansion (15) of the correlation part of Ω in RPA.

It is useful to separate (14) into the first-order exchange part (5) and correlation part $\delta\Omega_{corr}$. In order to obtain analytical results, we expand $\delta\Omega_{corr}$ in powers of $1/\Lambda$ up to Λ^{-2}:

$$\delta\Omega_{corr} = \frac{S|\mu|^3}{4\pi^2 v_F^2}\left\{a(\alpha_{gr})\ln\Lambda + c(\alpha_{gr}) + \frac{b(\alpha_{gr})}{\Lambda^2}\right\}, \quad (15)$$

where $\alpha_{gr} = ge^2/\varepsilon v_F$. The functions $a(\alpha_{gr})$, $b(\alpha_{gr})$ and $c(\alpha_{gr})$, being smooth, can be easily tabulated and approximated in the physically accessible range $0 \le \alpha_{gr} \lesssim 10$ (see Fig. 4). Our results for $\delta\Omega_{corr}$ are close to those given in [11, 39, 48].

From (1) and (15) we get the correlation correction

$$\delta n_{corr} = -\,\mathrm{sgn}(\mu)\frac{\mu^2}{4\pi^2 v_F^2}\left\{3a(\alpha_{gr})\ln\Lambda + 3c(\alpha_{gr}) - a(\alpha_{gr}) + \frac{5b(\alpha_{gr})}{\Lambda^2}\right\} \quad (16)$$

to the electron density $n = n_0 + \delta n_1 + \delta n_{corr}$ in RPA.

Note that the presented RPA is not self-consistent. The Luttinger-Ward theorem can be used to find Ω in the self-consistent RPA, which involves all diagrams of Fig. 3 with the diagrammatic series from Fig. 2 inside each loop, i.e. all diagrams without vertex corrections. All calculated quantities (Green functions, self-energy parts, thermodynamic potential) are consistent among themselves in this approximation. For example, calculation of the electron density at given μ through (1) or by solving the off-shell Dyson equation $\mu = \epsilon_{p_F,\mathrm{sgn}(n)} + \Sigma_{p_F,\mathrm{sgn}(n)}(\mu)$ (see [49]) will yield, unlike usual RPA, the same results when RPA is treated self-consistently. However, solving a complicated integral equation for the self-energy is required in the this case.

III. ANALYSIS OF EXPERIMENTAL DATA

The basic effect of electron interactions, considered in this article, is a deviation of the dependence $n(\mu)$ from its noninteracting form (4). This effect can be analyzed in terms of the renormalized Fermi velocity

$$v_F^* = |\mu|/p_F, \quad (17)$$

deviating from v_F in presence of interactions, or in terms of quantum capacitance C_Q, which is proportional to $dn/d\mu$. In this article, we use (see also [6, 14]) the term "renormalized Fermi velocity" in the meaning of the thermodynamic Fermi velocity (17), though sometimes this term is referred to the group velocity of quasiparticles on the Fermi surface, as discussed in [9].

Our calculations depend on two parameters: the bare Fermi velocity v_F and the environmental dielectric constant ε. To estimate them, we analyze experimental data on measured C_Q or v_F^* within HFA and RPA, described in the previous section. For our analysis, we use the data from four recent experimental works [6–8, 18], where the measured v_F^* [6, 18] or C_Q [7, 8] were reported.

In all our calculations, we use, following [13, 50], the cutoff momentum $p_c = 1.095\,\text{Å}^{-1}$, found by equating the density of valence band electrons $2/S_0$ to $gp_c^2/4\pi$, where $S_0 = 5.24\,\text{Å}^2$ is the area of graphene elementary cell.

We employ the following fitting procedures: first, we take the actual values of ε, determined by the substrate material in the experimental setup of each analyzed work [6–8, 18], and obtain v_F through the least square fittings of the measured v_F^* or C_Q with RPA theoretical formulas. Assuming that RPA appropriately takes into account both exchange and correlation effects (see also [20, 45]), the resulting values of v_F are expected to be generally adequate.

Second, we take these values of v_F and fit the same experimental data in HFA, obtaining new effective values of ε. These quantities turn out to be systematically larger, than the actual material values of ε, because the screening of the Coulomb interaction, present in RPA and now absent in HFA, should be mimicked by a stronger environmental screening.

The parameters v_F and ε, resulting from our fittings, are collected in Table I together with the authors' own estimates. The corresponding experimental points and theoretical curves are shown in Figs. 5 and 6. The comments on each of the considered experimental papers [6–8, 18], followed by a short discussion, are given below.

In the work [6] the capacitance C between AuTi gate electrode and graphene flake, encapsulated in hexagonal boron nitride (hBN), was accurately measured as a function of the gate voltage V_g. Then $C(V_g)$ was integrated

Experiment	Authors' fit		RPA fit		HFA fit	
	v_F	ε	v_F	ε	v_F	ε
Yu et al. [6]	0.850	8	0.892	4.5	0.892	9.01
Chae et al. [18]	0.957	3.15	0.910	3.15	0.910	8.45
Kretinin et al. [7]	1	—	1.039	4.5	1.039	14.04
Chen et al. [8]	0.957	4.14	1.386	4.14	1.386	9.07

TABLE I: Fitting parameters for the experimental data on quantum capacitance and renormalized Fermi velocity, determined by the authors of the corresponding papers and found in our study in HFA and RPA. The RPA values of ε are taken according to experimental conditions, and v_F is given in the units 10^6 m/s.

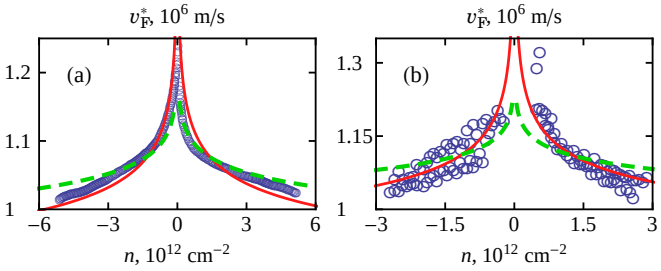

FIG. 5: Experimental data (blue circles) from [6] (a) and [18] (b) on renormalized Fermi velocity v_F^* as a function of electron density n, fitted in the Hartree-Fock (dashed line) and random phase (solid line) approximations. The data from [6] are recalculated with the additional electron density.

to obtain the electron density:

$$n(V_g) = \frac{1}{eS}\int_0^{V_g} C(V_g')\, dV_g'. \qquad (18)$$

The independently determined classical (or geometrical) capacitance per unit area C_C allowed then to obtain the chemical potential $\mu = eV_g - e^2 n/C_C$ and hence v_F^* (17). Using the first-order renormalization group result [19]

$$\frac{v_F^*}{v_F} = 1 + \frac{\alpha_{gr}}{8}\ln\frac{n_c}{|n|}, \qquad (19)$$

the effective background dielectric constant $\varepsilon = 8$ was obtained in [6] (the assumed cutoff density $n_c = 10^{15}\,\mathrm{cm}^{-2}$ corresponds to $p_c = 0.56\,\text{Å}^{-1}$). This ε is much larger than the actual dielectric constant $\varepsilon = 4.5$ of hBN, as expected in the first-order approximation, neglecting the screening.

The data on $v_F^*(n)$, presented in [6], demonstrate strong asymmetry and anomalous behavior near CNP, which are not commented by the authors. We suggest a possible explanation of this anomaly that some nonzero charge is present on graphene even at zero voltage due to impurities or parasitic external voltage. This excess charge appears as an integration constant in the right hand side of (18).

Assuming the additional charge density, equivalent to the electron density $\Delta n = -1.5\times10^9\,\mathrm{cm}^{-2}$ and recalculating the dependence $v_F^*(n)$, we managed to improve substantially agreement between the experiment [6] and our theoretical curves, as shown in Fig. 5(a). The both approximations reproduce the experimental points fairly well.

In [18] a graphene sample, placed on a hBN layer on top of oxidized silicon, was studied with the scanning tunneling spectroscopy in magnetic field. The electron and hole renormalized Fermi velocities were extracted from Landau level energies at different points of the sample, chosen inside electron and hole puddles. The authors fit the dependence $v_F^*(n)$ by an approximate RPA formula using the effective background dielectric constant $\varepsilon = (1+5.3)/2 \approx 3.15$, which originates as a half-sum of the dielectric constants of air and hBN-SiO_2 substrate layer. Our fittings of the data from [18], based on this dielectric constant, are shown in Fig. 5(b).

The work [7] is focused mainly on electron-hole asymmetry, however measurements of quantum capacitance were carried out there on high-quality graphene samples in the experimental setup, very similar to that in [6]. The results of the fitting, based on the hBN dielectric constant $\varepsilon = 4.5$, are shown in Fig. 6(a). Generally a quantum correction to the classical capacitance in this case is rather small, except the immediate vicinity of CNP, as shown in the inset.

In the work [8] the inverse compressibility κ^{-1} was measured as a function of electron density in graphene samples on SiO_2 substrate, covered by Y_2O_3 insulating layer. The data at $|n| < 0.3\times10^{12}\,\mathrm{cm}^{-2}$ were excluded from our analysis because of distorting effects of disorder, appreciable at these concentrations.

The authors of [8] adopt $v_F = 0.957\times10^6\,\mathrm{m/s}$ from [18] and use the effective dielectric constant $\varepsilon = (3.9 + 4.38) = 4.14$ to reproduce the measured κ^{-1} with the first-order expression, similar to (19). We replotted the data on κ in terms of quantum capacitance C_Q (see (2)) and show our fits, based on $\varepsilon = 4.14$, in Fig. 6(b). As demonstrated in the inset, a quantum correction to the classical capacitance is significant.

Looking at Table I and comparing the values of ε, taken according to the experimental conditions [6–8, 18] and then used in RPA fit, with those obtained via HFA fit, we see, as discussed above, that in the latter case ε is larger by 4.5–5.5 (except the case of [7], where it is larger by 9.5 by unknown reason). This difference, however, exceeds that following from the simple estimate [6] $\varepsilon_{\text{eff}} = \varepsilon + \pi g e^2/8v_F \approx \varepsilon + 3.46$, based on a static interband screening [47].

One can also note the anomalously high values of v_F,

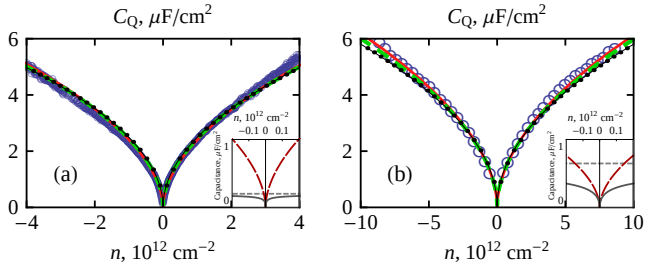

FIG. 6: Experimental data (blue circles) from [7] (a) and [8] (b) on quantum capacitance of graphene C_Q as a function of electron density n, fitted in the noninteracting model (dotted line) and in the Hartree-Fock (dashed line) and random phase (solid line) approximations. Insets: classical (dashed line), quantum (broken line, RPA fit) and total (solid line) capacitances per unit area versus electron density n.

obtained by fitting the data from [8]. Even within the authors' theoretical model, the best agreement with the experimental data is achieved at $v_F = 1.115 \times 10^6$ m/s, while the estimate $v_F = 0.957 \times 10^6$ m/s, assumed in [8], provides the values of κ^{-1}, which are smaller than the experimental ones. Perhaps the source of this anomaly is underestimated classical capacitance, used to extract the compressibility from total capacitance.

Lastly, quantum capacitance C_Q, in contrast to v_F^*, does not qualitatively change its dependence on n when interactions are switched on (see Fig. 8(a) in the next section). As a consequence, the experimental points on C_Q can be well described by the noninteracting dependence $C_Q = e^2\sqrt{g|n|/\pi v_F^2}$ with $v_F = 1.104 \times 10^6$ m/s, $\varepsilon = 4.5$ for the data from [7] and $v_F = 1.496 \times 10^6$ m/s, $\varepsilon = 4.14$ for the data from [8] (see Fig. 6).

IV. MANY-BODY EFFECTS OF COULOMB INTERACTIONS ON CHARACTERISTICS OF THE ELECTRON GAS

To calculate the quantum capacitance and the renormalized Fermi velocity of the electron gas in graphene, we choose the value $v_F \approx 0.9 \times 10^6$ m/s of the bare Fermi velocity, consistent with most of the data in Table I. We also take three characteristic values of the background dielectric constant, controlling an interaction strength: $\varepsilon = 1$ (suspended graphene), $\varepsilon = 4.5$ (graphene, encapsulated in hBN) and $\varepsilon = 8$ (graphene in a strongly screening environment).

To get an additional insight into results, we consider the kinetic E_{kin} and Coulomb interaction E_{int} energies of the electron gas, which can be found on the basis of the grand canonical ensemble as: $E_{kin} = v_F(\partial\Omega/\partial v_F)$, $E_{int} = e^2(\partial\Omega/\partial e^2)$. These energies, calculated for the ideal Dirac electron gas and for the interacting gas in different approximations, are shown in Fig. 7. The quantum capacitance and renormalized Fermi velocity, calculated under the same conditions, are shown in Fig. 8. FOA provides reasonable results only in a weak-interacting regime ($\varepsilon \gg 1$), thus its results are not shown at $\varepsilon = 1$. Even at $\varepsilon = 4.5$ it shows such artifacts as multiple-valuedness of $E_{kin}(n)$, $E_{int}(n)$, $\mu(n)$ and negative compressibility and C_Q near CNP.

In contrast to a usual electron gas with negative exchange energy, the electron exchange self-energy in graphene (8) is positive due to its chirality [48]. Therefore the exchange effects in graphene tend to increase v_F^*, as seen in Fig. 8(a) in FOA and HFA. As a consequence, C_Q becomes smaller (Fig. 8(b)), because this quantity reflects an effective density of states, which decreases as v_F^* increases (note that the interaction-induced change in C_Q can be essentially diminished by a proper choice of the fitting parameter v_F within the non-interacting model, as seen in Fig. 6).

For the same reason, the interaction energy E_{int}, consisting of exchange energies of individual electrons, is positive in FOA and HFA (Fig. 7(b)). The kinetic energy E_{kin} decreases in FOA due to decreasing density (Fig. 7(a)). In HFA it does not change in comparison with the non-interacting regime at the same density, because in the both cases the ground state wave function is the same Slater determinant. Generally HFA provides more plausible and moderate results than FOA even at $\varepsilon \gg 1$, which indicates importance of the self-consistent treatment of the interactions.

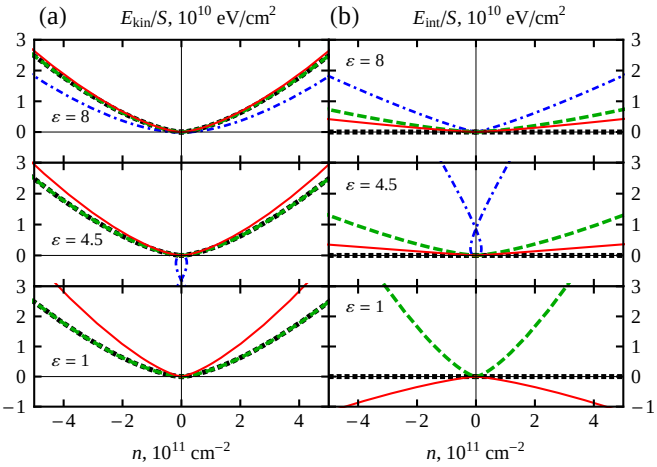

FIG. 7: Kinetic (a) and interaction (b) energies of the electron gas in graphene, calculated as functions of electron density n at different dielectric constants ε in the noninteracting regime (dotted line) and in the first-order (dash-dotted line), Hartree-Fock (dashed line) and random phase (solid line) approximations.

The difference between RPA and FOA results demonstrates correlation effects. As is known, electrons in the correlated electron liquid tend to be located in average farther from each other in comparison with the mean field picture, thus the interaction energy decreases. At the same time, the kinetic energy increases because of this additional correlated motion. The both of these effects are seen in Fig. 7. From the other point of view, the correlations partly compensate the exchange effects [11, 39] via screening of the Coulomb interaction. This can be seen in Fig. 8 at $\varepsilon = 4.5$ and 8, where the RPA curves are situated between noninteracting and HFA (or FOA) curves. However, at $\varepsilon = 1$ the correlation effects, which are at least quadratic in α_{gr}, can even overcompensate the linear in α_{gr} exchange effects, resulting in the negative interaction energy (Fig. 7(b)) and increased quantum capacitance (Fig. 8(a)).

V. DISORDER

A random disorder potential $V(\mathbf{r})$, arising in graphene sample due to substrate charge impurities and corrugations, leads to formation of a spatially varying electron density pattern, emerging as electron and hole puddles

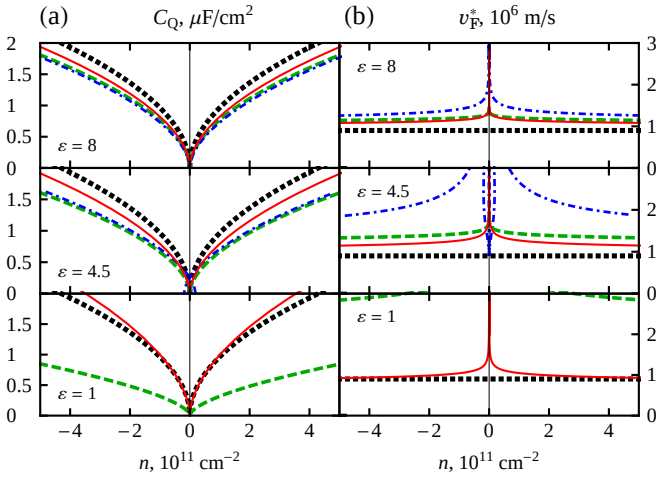

FIG. 8: Quantum capacitance C_Q (a) and renormalized Fermi velocity v_F^* (b), calculated as functions of electron density n at different dielectric constants ε in the noninteracting regime (dotted line) and in the first-order (dash-dotted line), Hartree-Fock (dashed line) and random phase (solid line) approximations.

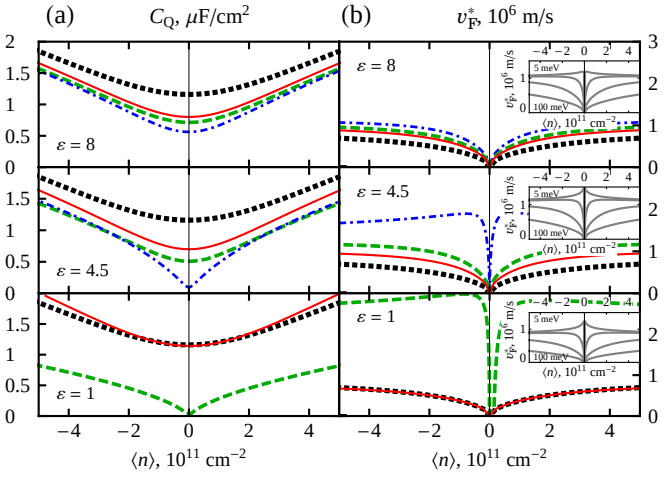

FIG. 9: The same quantities as in Fig. 8, calculated as functions of the average electron density $\langle n\rangle$ in the Gaussian disorder potential with the spread $s = 50$ meV. Insets in (b): v_F^*, calculated in RPA as a function of $\langle n\rangle$ with the following values of s (from top to bottom): 5, 20, 50 and 100 meV.

near CNP [4, 18, 21–23]. Typical size of the puddles, observed in recent experiments, is 10–20 nm [18, 21, 22]. Thus the local density approximation, proposed and used [23, 29–31, 33] to calculate the compressibility and quantum capacitance of disordered graphene, is applicable at the carrier densities $|n| > 10^{11}$ cm^{-2}, when $p_F^{-1} \lesssim 15$ nm.

In this approximation we assume that the local chemical potential $\mu_{\rm loc}(\mathbf{r})$ is established in each region of a graphene sample in such a way so that the total electrochemical potential $\mu = V(\mathbf{r}) + \mu_{\rm loc}(\mathbf{r})$ is constant throughout the sample. Following [23, 29–33], we assume the Gaussian distribution of areas of such regions:

$$\rho(V) = \frac{1}{\sqrt{2\pi}s} e^{-V^2/2s^2}. \qquad (20)$$

Thus the experimentally observed electron density in graphene sample can be calculated as a spatial average of the local density $n(\mu_{\rm loc}) = n(\mu - V)$:

$$\langle n(\mu)\rangle = \int \rho(V) n(\mu - V)\, dV. \qquad (21)$$

The spread s in (20) can be related to the average charge carrier density $|n|$ at $T \to 0$, calculated from (21)–(20) at CNP: $\langle |n|\rangle = s^2/\pi v_F^2$. The values of s, reported in the experiments with graphene on SiO_2 [4, 8, 21, 23–26, 28, 29] and other substrates [22, 27], or calculated from the corresponding residual carrier densities, range from 10 to 130 meV. Therefore we assume $s = 50$ meV to be a typical disorder strength. Similar values are considered in theoretical works [30–33].

The quantum capacitance and renormalized Fermi velocity, calculated taking into account disorder by replacing $n(\mu)$ in (2) and (17) with $\langle n(\mu)\rangle$, are shown in Fig. 9. The major effect of disorder on C_Q is its smearing, leading to appearance of a nonzero C_Q at CNP, where $C_Q = 0$ in the clean limit (see Fig. 8(a)). At the same time, v_F^* demonstrates quite unexpected behavior: it falls to zero in the immediate vicinity of CNP. This is due to the fact that the resulting finite density of states at CNP $\langle D(E=0)\rangle = s/(2^{1/2}\pi^{3/2}v_F^2)$ implies $\langle n\rangle \propto \mu$, so that $v_F^* \propto |\mu|^{1/2} \propto |\langle n\rangle|^{1/2}$. Perhaps this can explain the anomalous dip of v_F^* at CNP, observed in [6].

An influence of disorder of various strength on v_F^* is shown in the inset of Fig. 9(b). As seen, the peak near CNP still survives at $s = 5$ meV and disappears at $s = 20$ meV. According to our estimates, this disappearance occurs at $s = 12$–15 meV at each value of ε.

VI. CONCLUSIONS

We have considered the many-body effects of Coulomb interactions on such observable quantities of graphene as the quantum capacitance C_Q, compressibility κ and renormalized (thermodynamic) Fermi velocity v_F^*. Three approximations (FOA, HFA and RPA) are analyzed and applied for massless Dirac electrons.

The recent experimental data on v_F^* [6, 18] and C_Q [7, 8] were analyzed in RPA, with the bare Fermi velocity $v_F \approx 0.9 \times 10^6$ m/s obtained as the result of the least square fitting. The same experimental data were described by HFA as well, but with larger values of the background dielectric constant that simulates the screening, absent in this approximation.

Our main conclusions, concerning the influence of Coulomb interactions on C_Q, v_F^*, and kinetic and interaction energies of the electron gas in graphene, are the following:

a) Kinetic energy increases in presence of the interactions (in RPA) due to correlated motion of electrons.

b) Interaction energy is positive due to the positive exchange energy (as opposed to a usual electron gas) [48], while it somewhat reduces in RPA due to the correlations, which partly compensate the exchange.

c) The very demonstrative effect of the interactions is the renormalization of $v_{\rm F}^*$ to higher values, most prominent near CNP. In RPA, $v_{\rm F}^*$ increases by 50 % at lowest achievable carrier densities $n \sim 10^9\,{\rm cm}^{-2}$ and by 10–20 % at moderate densities $n \sim 10^{11}$–$10^{12}\,{\rm cm}^{-2}$.

d) The quantum capacitance $C_{\rm Q}$ decreases in presence of interactions by 10–15 % due to effective reduction of the density of states at higher $v_{\rm F}^*$. However, generally it changes only quantitatively, retaining the same form $C_{\rm Q} \propto \sqrt{n}$ as in the noninteracting model. That is why experimentally measured $C_{\rm Q}$ and κ are often successfully described in the noninteracting model [4, 23, 24, 26, 28, 29, 31, 33, 51], but with the higher Fermi velocity $v_{\rm F} \approx 1.1 \times 10^6\,{\rm m/s}$.

The considered theoretical models can be easily generalized to take into account a disorder fluctuating potential in the local density approximation. Calculations of $C_{\rm Q}$ in the model of Gaussian fluctuations with the typical spread 50 meV show formation of a nonzero $C_{\rm Q}$ at CNP, in agreement with experiments. On the contrary, $v_{\rm F}^*$ acquires a dip at CNP, which can even override the logarithmic interaction-induced peak at disorder potential spread exceeding 12–15 meV. Note should be taken that we expect such disorder-induced dip only in the thermodynamic Fermi velocity obtained in e.g. quantum capacitance or cyclotron mass measurements, but not in the quasiparticle Fermi velocity, obtained in measurements of single-particle characteristics.

Finally we can note that studies of graphene quantum capacitance are important for its electronic applications, because $C_{\rm Q}$ dominates in case of ultrathin oxide layer between graphene and a gate (see, e.g., [52–54]). In this case an additional screening by the metallic gate electrode can essentially affect the many-body corrections to $C_{\rm Q}$, as considered in [50].

The work of A.D.Z. was supported by RFBR, and the work of Y.E.L. and A.A.S. was supported by the HSE Basic Research Program.

[1] A.H. Castro Neto, F. Guinea, N.M.R. Peres, K.S. Novoselov, A.K. Geim, Rev. Mod. Phys. **81**, 109 (2009).

[2] D.S.L. Abergel, V. Apalkov, J. Berashevich, K. Ziegler, T. Chakraborty, Adv. Phys. **59**, 261 (2010).

[3] V.N. Kotov, B. Uchoa, V.M. Pereira, F. Guinea, A.H. Castro Neto, Rev. Mod. Phys. **84**, 1067 (2012).

[4] J. Martin, N. Akerman, G. Ulbricht, T. Lohmann, J.H. Smet, K. von Klitzing, A. Yacoby, Nature Phys. **4**, 144 (2008).

[5] D.S.L. Abergel, P. Pietiläinen, T. Chakraborty, Phys. Rev. B **80**, 081408(R) (2009).

[6] G.L. Yu, R. Jalil, B. Belle, A.S. Mayorov, P. Blake, F. Schedin, S.V. Morozov, L.A. Ponomarenko, F. Chiappini, S. Wiedmann, U. Zeitler, M.I. Katsnelson, A.K. Geim, K.S. Novoselov, D.C. Elias, PNAS **110**, 3282 (2013).

[7] A. Kretinin, G.L. Yu, R. Jalil, Y. Cao, F. Withers, A. Mishchenko, M.I. Katsnelson, K.S. Novoselov, A.K. Geim, F. Guinea, Phys. Rev. B **88**, 165427 (2013).

[8] X. Chen, L. Wang, W. Li, Y. Wang, Z. Wu, M. Zhang, Y. Han, Y. He, N. Wang, Nano Res. **6**, 619 (2013).

[9] E.H. Hwang, B.Y.-K. Hu, S. Das Sarma, Phys. Rev. Lett. **99**, 226801 (2007).

[10] Q. Li, E.H. Hwang, S. Das Sarma, Phys. Rev. B **84**, 235407 (2011).

[11] Y. Barlas, T. Pereg-Barnea, M. Polini, R. Asgari, A.H. MacDonald, Phys. Rev. Lett. **98**, 236601 (2007).

[12] R. Asgari, M.M. Vazifeh, M.R. Ramezanali, E. Davoudi, B. Tanatar, Phys. Rev. B **77**, 125432 (2008).

[13] D.E. Sheehy, J. Schmalian, Phys. Rev. Lett. **99**, 226803 (2007).

[14] Z.Q. Li, E.A. Henriksen, Z. Jiang, Z. Hao, M.C. Martin, P. Kim, H.L. Stormer, D.N. Basov, Nature Phys. **4**, 532 (2008).

[15] D.C. Elias, R.V. Gorbachev, A.S. Mayorov, S.V. Morozov, A.A. Zhukov, P. Blake, L.A. Ponomarenko, I.V. Grigorieva, K.S. Novoselov, F. Guinea, A.K. Geim, Nature Phys. **7**, 701 (2011).

[16] D.A. Siegel, C.-H. Park, C. Hwang, J. Deslippe, A.V. Fedorov, S.G. Louie, A. Lanzara, PNAS **108**, 11365 (2011).

[17] A. Luican, G. Li, E.Y. Andrei, Phys. Rev. B **83**, 041405(R) (2011).

[18] J. Chae, S. Jung, A.F. Young, C.R. Dean, L. Wang, Y. Gao, K. Watanabe, T. Taniguchi, J. Hone, K.L. Shepard, P. Kim, N.B. Zhitenev, J.A. Stroscio, Phys. Rev. Lett. **109**, 116802 (2012).

[19] J. González, F. Guinea, M.A.H. Vozmediano, Nucl. Phys. B **424**, 595 (1994).

[20] E. Barnes, E.H. Hwang, R.E. Throckmorton, S. Das Sarma, Phys. Rev. B **89**, 235431 (2014).

[21] Y. Zhang, V.W. Brar, C. Girit, A. Zettl, M.F. Crommie, Nature Phys. **5**, 722 (2009).

[22] S.C. Martin, S. Samaddar, B. Sacépé, A. Kimouche, J. Coraux, F. Fuchs, B. Grévin, H. Courtois, C.B. Winkelmann, arXiv:1304.1183v3.

[23] E.M. Hajaj, O. Shtempluk, V. Kochetkov, A. Razin, Y.E. Yaish, Phys. Rev. B **88**, 045128 (2013).

[24] Z. Chen, J. Appenzeller, IEEE El. Dev. Meeting Tech. Digest **21.1**, 509 (2008).

[25] S. Dröscher, P. Roulleau, F. Molitor, P. Studerus, C. Stampfer, K. Ensslin, T. Ihn, Appl. Phys. Lett. **96**, 152104 (2010).

[26] J. Xia, F. Chen, J. Li, N. Tao, Nature Nanotech. **4**, 505 (2009).

[27] J.L. Xia, F. Chen, J.L. Tedesco, D.K. Gaskill, R.L. Myers-Ward, C.R. Eddy, D.K. Ferry, N.J. Tao, Appl. Phys. Lett. **96**, 162101 (2010).

[28] L.A. Ponomarenko, R. Yang, R.V. Gorbachev, P. Blake, A.S. Mayorov, K.S. Novoselov, M.I. Katsnelson, A.K. Geim, Phys. Rev. Lett. **105**, 136801 (2010).

[29] H. Xu, Z. Zhang, L.-M. Peng, Appl. Phys. Lett. **98**,

133122 (2011).
[30] G.S. Kliros, Rom. J. Inf. Sci. Technol. **13**, 332 (2010).
[31] G.I. Zebrev, E.V. Melnik, A.A. Tselykovskiy, arXiv:1011.5127.
[32] Q. Li, E.H. Hwang, S. Das Sarma, Phys. Rev. B **84**, 115442 (2011).
[33] D.S.L. Abergel, E.H. Hwang, S. Das Sarma, Phys. Rev. B **83**, 085429 (2011).
[34] A.A. Abrikosov, L.P. Gorkov, I.E. Dzyaloshinskii, *Quantum field theoretical methods in statistical physics* (Pergamon Press, Oxford, 1965), p. 128.
[35] G.D. Mahan, *Many-particle physics* (Plenum Press, New York, 1990), p. 179.
[36] N.M.R. Peres, F. Guinea, A.H. Castro Neto, Phys. Rev. B **72**, 174406 (2005).
[37] E. Rossi, S. Das Sarma, Phys. Rev. Lett. **101**, 166803 (2008).
[38] G. Borghi, M. Polini, R. Asgari, A.H. MacDonald, Solid State Commun. **149**, 1117 (2009).
[39] M. Polini, A. Tomadin, R. Asgari, A.H. MacDonald, Phys. Rev. B **78**, 115426 (2008).
[40] J.M. Luttinger, J.C. Ward, Phys. Rev. **118**, 1417 (1960).
[41] J.M. Luttinger, Phys. Rev. **119**, 1153 (1960).
[42] V.N. Kotov, B. Uchoa, A.H. Castro Neto, Phys. Rev. B **80**, 165424 (2009).
[43] S.M. Apenko, D.A. Kirzhnits, Yu.E. Lozovik, Phys. Lett. A **92**, 107 (1982).
[44] S. Das Sarma, B.Y.-K. Hu, E.H. Hwang, W.-K. Tse, arXiv:0708.3239v3.
[45] J. Hofmann, E. Barnes, S. Das Sarma, Phys. Rev. Lett. **113**, 105502 (2014).
[46] B. Wunsch, T. Stauber, F. Sols, F. Guinea, New J. Phys. **8**, 318 (2006).
[47] E.H. Hwang, S. Das Sarma, Phys. Rev. B **75**, 205418 (2007).
[48] M. Polini, R. Asgari, Y. Barlas, T. Pereg-Barnea, A.H. MacDonald, Solid State Commun. **143**, 58 (2007).
[49] S. Das Sarma, E.H. Hwang, Phys. Rev. B **87**, 045425 (2013).
[50] R. Asgari, M.I. Katsnelson, M. Polini, Ann. Phys. (Berlin) **526**, 359 (2014).
[51] F. Giannazzo, S. Sonde, V. Raineri, E. Rimini, Nano Lett. **9**, 23 (2009).
[52] K.N. Parrish, D. Akinwande, Appl. Phys. Lett. **101**, 053501 (2012).
[53] H. Xu, Z. Zhang, Z. Wang, S. Wang, X. Liang, L.-M. Peng, ACS Nano **5**, 2340 (2011).
[54] G.I. Zebrev, A.A. Tselykovskiy, D.K. Batmanova, E.V. Melnik, IEEE Trans. El. Dev. **60**, 1799 (2013).